IE : 617 - PROD.TYPE: COM ED: MARIAMMA/BALA
pp.1–17 (col.fig.: 3, 4, 5) PAGN: SCAN: SHOBHA/S.V. LAKSHMI

PERGAMON International Journal of Impact Engineering 0 (2001) 1–17

INTERNATIONAL JOURNAL OF IMPACT ENGINEERING
www.elsevier.com/locate/ijimpeng

A computational study of the influence of thermal softening on ballistic penetration in metals

S. Yadav*, E.A. Repetto, G. Ravichandran, M. Ortiz

Graduate Aeronautical Laboratories, California Institute of Technology, Pasadena, CA 91125, USA

Received 21 May 1999; received in revised form 16 February 2001

Abstract

A two-dimensional axisymmetric computational study of the penetration of a tungsten heavy alloy (WHA) rod into a 6061-T6 aluminum target has been performed using a Lagrangian formulation. Adaptive remeshing has been used to alleviate the problem of excessive distortion of elements which occurs during large deformation studies (such as ballistic penetration). Strain hardening, strain-rate hardening and thermal softening in both the penetrator and target materials are taken into full consideration. The computed depth of penetration (DOP), residual penetrator length and maximum crater diameter match very well the experimental results reported by Yadav and Ravichandran (Int. J. Impact Eng., Submitted for publication) for an impact velocity of 1100 m/s. Computer simulations reveal that in the absence of failure mechanisms (such as shear banding), introduction of thermal softening in the penetrator material decreases its depth of penetration in a metal target, when compared to a penetrator material which does not soften thermally. These results are in contrast to the recent work of Rosenberg and Dekel (Int. J. Impact Eng. 13(1998) 283–296) and a plausible explanation for this discrepancy is presented.

1. Introduction

The computational modeling of ballistic penetration phenomenon still remains an active area of endeavor. Very large strains, strain rates, pressures and temperatures are obtained in the penetrator and target materials during the penetration process. The constitutive behavior of materials at such large strain rates and at elevated temperatures is often not well characterized. Similarly the failure mechanisms which are operative in the target and penetrator materials undergoing rapid deformations under very high, superimposed hydrostatic pressures and at

*Corresponding author. Current address: Fermilab, MS 316, P.O. Box 500, Batavia, IL 60510, USA. Tel.: +1-630-840-6490; fax: +1-630-840-8036.

E-mail address: syadav@fnal.gov (S. Yadav).

PII: S0734-743X(01)00008-2

elevated temperatures are not well understood. Simplified constitutive assumptions about material behavior and failure are often made in the computer codes used to study ballistic penetration. For example, many studies reported in the literature have assumed either both or one of the penetrator/target material to be elastic, perfectly plastic and use an average value of the effective flow stress to account for dynamic effects. Similarly, several of the reported studies on ballistic penetration phenomenon did not incorporate effects of thermal softening for one or both of the penetrator/target materials. The accuracy of these computer codes is often limited by such simplifying assumptions. Therefore, it is necessary to understand the influence of material parameters such as the yield strength, strain and strain rate hardening, and thermal softening on ballistic performance.

The effect of target and penetrator material strength parameters on depth of penetration (DOP) in semi-infinite targets has been studied by several investigators. For example, Anderson et al. [1] performed computer simulations of the penetration of tungsten alloy long-rod penetrators into armor steel targets at an impact velocity of 1.5 km/s. They observed that while the DOP is very sensitive to the target strength, it is quite insensitive to small differences in the projectile strength. Similar conclusions have been reported by Hohler and Stilp [2] who showed that penetration is much more sensitive to target strength and that the strength of the penetrator had minor effects on its performance. The effect of strain hardening and strain-rate hardening on depth of penetration has also been investigated [3,4]. However, note that most of the studies reported in the literature did not incorporate the combined effect of thermal softening of both the penetrator and target materials on the ballistic behavior. The effect of thermal softening of the target material (but not the penetrator material) has been examined by Anderson and Walker [4], who reported that the final depth of penetration computed with this effect included lied within the scatter of the experimental data. Some counter-intuitive results such as decrease in the normalized penetration length (P/L) with an increase in the projectile strength have been reported by some researchers [5,6]; a phenomenon which is observed to disappear when thermal softening effects are accounted for [7]. Similarly, contradictory result such as increase in the depth of penetration with the introduction of thermal softening in the penetrator material has been reported [7]. It has been suggested [8] that the Taylor–Quinney coefficient β, which dictates the fraction of plastic work that is converted into heat, vanishes under the extreme conditions of strain rate and temperature (which prevail during ballistic penetration).

The objective of this paper is to investigate the role of constitutive parameters, especially the influence of thermal softening in the penetrator and target materials on the penetration of a cylindrical penetrator into a metal target. As a benchmark test, we first simulate one of the experiments of Yadav and Ravichandran [9] involving penetration of a flat-nose, cylindrical tungsten heavy alloy (WHA) penetrator into a 6061-T6 aluminum target at an impact velocity of 1100 m/s. Note that the penetration resistance of 6061-T6 aluminum targets against WHA penetrators is also of interest due to its use in lightweight armor applications and as a backing material for ceramic armor [9]. A full account is taken of the strain and strain-rate hardening and thermal softening in both the penetrator and the target material in these simulations. The material parameters for the WHA and 6061-T6 aluminum were obtained from quasistatic, dynamic and thermal softening data (obtained experimentally) reported in literature. The depth of penetration, residual penetrator length and maximum crater diameter obtained from numerical simulations are compared with the experimental data. We also conduct a parametric analysis to investigate the influence of thermal softening in the penetrator and target materials on their ballistic performance.

Section 2 describes briefly the finite element model used in this study. The constitutive framework adopted in the code is presented in Section 3, which is followed by a description of the material properties used for the WHA and 6061-T6 aluminum in Section 4. Section 5 presents the results of the numerical simulations. The influence of coefficient of friction between the penetrator/target surfaces and that of thermal softening in the penetrator and target materials on ballistic penetration is also presented in Section 4. Finally, Section 6 summarizes the main conclusions derived from this study.

2. Finite element model

PEN2D [10], an axisymmetric Lagrangian finite element code with adaptive remeshing was used in this study. A Lagrangian formulation of dynamic deformations is utilized due to its simplicity in representing the balance equations of mass, momentum and energy. Note that one of the main limitations of a Lagrangian formulation for large deformation studies (such as those occurring in ballistic penetration) is the excessive distortion of the elements, which leads to unacceptably small time steps and numerical instability of the solution. We use continuous adaptive remeshing to alleviate the problem of element distortion [11]. The mesh adaption algorithm is based on an equal distribution of an activity indicator ($I_{\mathrm{e}} = \int_{\Omega_e} \sqrt{\frac{1}{2} d_{ij} d_{ij}}$ where d_{ij} is the rate of deformation tensor) in each body, which provides a basis for mesh refinement (coarsening) in regions of large (small) deformation gradients. To compute the new element sizes, the current sizes are scaled by a factor $\bar{I}_{\mathrm{e}}/I_{\mathrm{e}}$, where $\bar{I}_{\mathrm{e}}$ is the body average of I_{e}. This factor is constrained to be between 0.5 and 1.25 to avoid sudden changes in the mesh size distribution. Also, the final size of the elements is clamped to be between a user-specified upper and lower bounds. The adaptive meshing technique used here offers an attractive alternative to the erosion techniques used in other Lagrangian formulations [12], which require empirical determination of the erosion parameter (such as the equivalent plastic strain) through a fit between the calculated and experimental data. Different depths of penetration can be obtained as the erosion strain for deformed elements is varied [13]. By continuously refining the mesh at regions of large deformation gradients (such as the penetrator/target interface), adaptive remeshing prevents severe distortion of the elements which can cause inversion of the elements and hence numerical instability in the solution. Thus, adaptive remeshing removes the empiricism in the solution technique and hence computer simulations can be used as a predictive tool in penetration studies.

Fig. 1 shows an initial finite element mesh used for studying the normal impact of a tungsten heavy alloy penetrator against a 6061-T6 aluminum target. The problem is assumed to be axisymmetric and therefore a two-dimensional analysis suffices. Because of the symmetry of the problem, only half of the geometry needs to be modeled. The finite element mesh is comprised of six-noded composite triangular elements [14], with linear stress and strain interpolation, which are free of volumetric locking. The state variables are sampled at three quadrature points per element. The initial mesh consists of 2027 triangular elements and 4261 nodes. An advancing front method is utilized for automatic mesh generation. Adaptive meshing is achieved using an h-adaption strategy which keeps the order of the elements unchanged while seeking to improve the solution

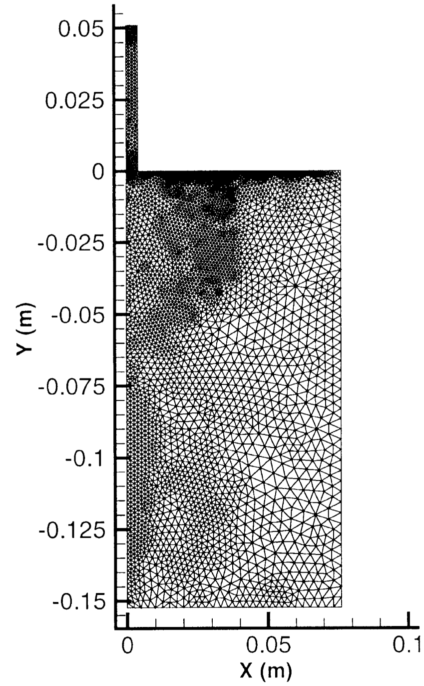

Fig. 1. An initial finite element mesh used for studying the impact of a cylindrical WHA penetrator against a 6061-T6 aluminum alloy target, at an impact velocity of 1100 m/s.

by adaptive mesh refinement and coarsening. Further details of the numerical implementation of mesh adaption can be found elsewhere [8]. An explicit contact/friction algorithm is used to represent contact between deformable bodies [8]. Note that mesh adaption furnishes a convenient means of ensuring that contact conditions are accurately accounted for. A second-order accurate central difference scheme is used to discretize in time the mechanical governing equations based on a lumped mass matrix.

Since ballistic penetration involves large deformations, a substantial amount of heat is generated due to plastic deformation and frictional sliding at the interfaces. The rate of heat supply due to plastic deformation is given by

$$s = \beta \dot{W}^{\mathrm{p}}, \tag{1}$$

where β is the Taylor–Quinney coefficient and $\dot{W}^{\mathrm{p}}$is the plastic power per unit deformed volume. On the other hand, rate at which heat is generated at frictional contact is given by the scalar product of two vectors as

$$h = -t \circ \|v\|, \tag{2}$$

where t is the contact traction and $\|v\|$ is the jump in velocity across the contact. Note that the contact traction t cannot exceed the maximum Coulomb frictional resistance between the contact surfaces. The heat generated at frictional contact is apportioned between the contacting bodies as

$$\frac{h_1}{h_2} = \frac{\sqrt{k_1 \rho_2 c_2}}{\sqrt{k_2 \rho_1 c_1}}, \tag{3}$$

where k_α, ρ_α and c_α ($\alpha = 1, 2$) are the thermal conductivity, mass density and heat capacity of the contacting bodies 1 and 2. This generated heat can have a significant influence on the mechanical behavior of the target and penetrator materials. Therefore, the mechanical and the thermal problem are fully coupled and a staggered procedure is adopted for this purpose. This involves assuming constant temperature during the mechanical step and constant heat generation during the thermal step. The discretized form of the energy balance equation is made up of a lumped capacitance matrix and is solved explicitly by resorting to forward Euler algorithm. Further details of the finite element code used in this study can be found in [8,10].

3. Constitutive model

The Cauchy stress tensor is decomposed into hydrostatic and deviatoric components,

$$\sigma_{ij} = -p\delta_{ij} + s_{ij}, \tag{4}$$

where p is the hydrostatic pressure and s_{ij} is the stress deviator. The compressive volumetric response is given by

$$p = K_1\mu + K_2\mu^2 + K_3\mu^3, \tag{5}$$

where $\mu = \mathrm{Log}(J)$, $J = \mathrm{Det}(\mathbf{F}) = \rho_o/\rho$ is the Jacobian of the deformation gradient tensor, $\mathbf{F}$ is the deformation gradient tensor, and K_1, K_2 and K_3 are polynomial constants. In addition, a small artificial bulk viscosity term is added to the hydrostatic pressure p to smear out the shock front over a region of constant width. This viscous pressure takes the form

$$q = b_1 \rho c_{\mathrm{d}} l \frac{\dot{J}}{J} - \rho \left(b_2 l \frac{\dot{J}}{J} \right)^2, \tag{6}$$

where b_1 and b_2 are constants, c_{d} is the dilatational wave speed, $\dot{J}/J$ is the volumetric strain rate and l is a typical element dimension.

A finite deformation plasticity based formulation is used to describe the deviatoric (shear) response of the target and penetrator materials. This assumes that the deformation gradient tensor $\mathbf{F}$ can be multiplicatively decomposed into elastic and plastic parts, $\mathbf{F}^{\mathrm{e}}$ and $\mathbf{F}^{\mathrm{p}}$, respectively. Thus,

$$\mathbf{F} = \mathbf{F}^{\mathrm{e}}\mathbf{F}^{\mathrm{p}}. \tag{7}$$

The plastic flow rule is expressed on an intermediate configuration (to satisfy the material frame indifference) and is given by

$$\dot{F}^{\mathrm{p}} F^{\mathrm{p}-1} = \dot{\varepsilon}^{\mathrm{p}} \bar{\mathbf{R}}(\bar{\mathbf{S}}, \bar{\mathbf{Q}}), \tag{8}$$

where $\dot{\varepsilon}^{\mathrm{p}}$ is an effective plastic strain rate, $\bar{\mathbf{R}}$ is the plastic flow direction, $\bar{\mathbf{S}}$ is the second Piola–Kirchoff stress tensor, and $\bar{\mathbf{Q}}$ denotes some suitable set of internal variables. Note that an overbar has been used to identify fields defined over the intermediate configuration.

The target and penetrator materials are represented by constitutive formulations incorporating strain hardening, strain-rate hardening, and thermal softening that occurs in these materials at the very high rates of loading that occur during ballistic penetration. A conventional viscoplastic power-law formulation is used to represent the rate sensitive flow behavior of both the target and penetrator materials. This power-law representation is akin to

$$\dot{\varepsilon}^{\mathrm{p}} = \dot{\varepsilon}_0^{\mathrm{p}}\left[\left(\frac{\bar{\sigma}}{g(\varepsilon^{\mathrm{p}})}\right)^m - 1\right] \quad \text{if } \bar{\sigma} > g(\varepsilon^{\mathrm{p}}) \tag{9a}$$

$$\dot{\varepsilon}^{\mathrm{p}} = 0 \quad \text{if } \bar{\sigma} \leqslant g(\varepsilon^{\mathrm{p}}), \tag{9b}$$

where $\bar{\sigma}$ is the effective von-Mises stress, g is the flow stress, ε^{p} is the effective plastic strain, $\dot{\varepsilon}_0^{\mathrm{p}}$ is a reference plastic strain rate, and m is the strain rate sensitivity exponent. The strain hardening in the material is represented by an equally conventional power hardening law in conjunction with Johnson and Cook's power thermal softening law, which gives

$$g = \sigma_{\mathrm{y}}\left(1 + \frac{\varepsilon^{\mathrm{p}}}{\varepsilon_0^{\mathrm{p}}}\right)^{1/n}\left[1 - \left(\frac{T - T_0}{T_{\mathrm{m}} - T_0}\right)^{\alpha}\right], \tag{10}$$

where n is the strain hardening exponent, $\varepsilon_0^{\mathrm{p}}$ is a reference plastic strain, T is the current temperature, T_0 is a reference temperature, T_{m} is the melting temperature, α is the thermal softening exponent, and σ_{y} is the reference yield stress at temperature T_0. Note that the thermal softening model employed here assumes that the material looses all its stress carrying capacity at its melting temperature.

4. Material properties

As a benchmark test, we performed computer simulations of one of the ballistic penetration experiment reported by Yadav and Ravichandran [9]. The experiment was performed at an impact velocity of 1100 m/s using a cylindrical tungsten heavy alloy (WHA) penetrator with a flat nose, with a length to diameter (L/D) ratio of 6 ($L = 50$ mm, $D = 8.43$ mm). The total mass of the penetrator was 50 g. The penetrator material had a density of 17.7 g/cm^3 and a chemical composition of 93 wt% tungsten, 5.6 wt% nickel and 1.4 wt% iron. The target was made of 6061-T6 aluminum cylinder of 152.4 mm diameter and of length equal to its diameter. The relevant mechanical constants, equation of state constants and thermal constants for the two materials are summarized in Tables 1–3. The experimentally observed depth of penetration for this case was 85 mm. Also the final residual penetrator length was observed to be 26 mm and the maximum crater diameter was 16 mm (see Run 9 in Table 4).

The strain and strain-rate hardening parameters for the 6061-T6 aluminum alloy were derived from the experimental results of Yadav et al. [15] obtained using a combination of servohydraulic testing machine, a compression Kolsky bar and a high strain rate pressure-shear plate impact facility. The thermal softening parameter α for the 6061-T6 aluminum alloy was obtained by

Table 1
Mechanical constants

Material	ρ (kg/m^3)	E (GPa)	ν	σ_y (GPa)	ε_0^p	n	$\dot{\varepsilon}_0^p$	m
6061-T6 Al	2700	69	0.33	0.276	0.001	13.5	1000	11.5
WHA	17700	345	0.29	1.35	0.0033	10.0	1000	8.0

Table 2
Equation of state constants

Material	K_1 (GPa)	K_2 (GPa)	K_3 (GPa)
6061-T6 Al	55.5	297.0	197.0
WHA	320.0	564.0	1053.0

Table 3
Thermal constants

Material	c (J/kg K)	k (W/mK)	T_0 (K)	T_m (K)	α	β
6061-T6 Al	896	167	298	853	0.5	1.0
WHA	138	120	298	1723	0.78	1.0

Table 4
Summary of the computational runs. Coefficient of friction $\mu = 0.2$ for the computational runs unless otherwise stated

	Run	Depth of penetration (mm)	Residual penetrator length (mm)	Maximum crater diameter (mm)
1.	No thermal softening in WHA & Al	104	40.0	10.6
2.	Thermal softening in Al alone ($\alpha = 1$, $\beta = 0$)	118	41.7	10.4
3.	Thermal softening in WHA alone ($\alpha = 1$, $\beta = 0$)	79	33.8	13.4
4.	Thermal softening in WHA alone ($\alpha = 1$, $\beta = 1$)	59	25.8	14.4
5.	Thermal softening in both WHA & Al ($\alpha = 1$, $\beta = 0$)	81	34.1	13.4
6.	Thermal softening in both WHA & Al ($\alpha = 1$, $\beta = 1$)	70	26.0	13.8
7.	Thermal softening in both WHA & Al (α and β as per Table 3)	79	26.0	14.8
8.	Thermal softening in both WHA & Al ($\mu = 0.01$, α and β as per Table 3)	83	26.0	14.8
9.	Experiment	85	26.0	16.0

fitting the Johnson–Cook thermal softening power law to the experimental data reported in Mark's handbook [16]. Note that the experimental data reported in [16] was obtained at quasistatic strain rates and the underlying assumption which we make is that the rate of thermal softening remains the same even at high strain rates. The equation of state constants for the

6061-T6 aluminum alloy were obtained by fitting LASL shock Hugoniot data [17] on 6061-T6 aluminum alloy with our constitutive representation (Eq. (5)).

The quasistatic mechanical properties for the tungsten heavy alloy (WHA) were provided by the manufacturer. However, there is no high strain rate or thermal softening data available for the particular tungsten heavy alloy used for the penetration experiments reported in [9]. Therefore, it was assumed that the strain and strain rate hardening and thermal softening in the WHA were same as that in a similar tungsten alloy (containing 91 wt% tungsten) investigated by Yadav and Ramesh [18]. Note that this is a good approximation of the real behavior since the strain-rate hardening and thermal softening in 90–93% by weight fraction tungsten alloys with a nickel–iron matrix is almost similar [4,18]. Also, there was no shock Hugoniot data available for the tungsten alloy used in the penetration experiments. Therefore, the equation of state constants for the tungsten alloy were assumed to be the same as that obtained by curve fitting experimental shock data on polycrystalline tungsten [17] with our constitutive representation (Eq. (5)).

The coefficient of friction μ between the two contacting surfaces was assumed to be 0.01. The Taylor–Quinney coefficient β, which dictates the fraction of plastic work that is converted into heat, was assumed to be equal to 1.0 for both materials. This appears to be a reasonable assumption for ballistic penetration which involves very large strains. Note that it has been shown by Hodowany et al. [19] that β approaches 1.0 for aluminum alloys for strains greater than 15%.

5. Results and discussion

5.1. Numerical simulation results

Fig. 2 presents the time sequence of penetration at four different instances of time, obtained from the simulations. Note that the use of adaptive meshing ensures that the mesh is fine near the penetrator/target interface (where large deformation gradients are present). Far away from the penetrator/target interface, the deformations and deformation gradients are small, and therefore the adaptive meshing algorithm results in the recombination of elements (coarsening of the mesh) in these regions. The main reason for resorting to adaptive coarsening is to prevent an excessive proliferation of elements resulting in runaway problem sizes. It is observed that the penetrator head mushrooms as it penetrates the target, whereas the target primarily undergoes radial expansion. Extremely large plastic deformations occur at the penetrator/target interface during the penetration process. The penetrator erodes as it penetrates deeper into the target and the velocity of the penetrator/target interface decreases with time. The penetrator finally comes to a stop and recoils slightly due to the stored elastic energy in the target. Table 4 provides the results of this computation as Run 8. The final depth of penetration observed from numerical simulations is 83 mm which matches fairly well with the experimentally measured value of 85 mm. The final residual penetrator length and the maximum crater diameter from numerical simulations are obtained as 26 and 14.8 mm, respectively. This again matches fairly well with the experimental measurements of 26 and 16 mm, respectively. The above calculations were repeated on a finer mesh to check for mesh convergence. The depth of penetration increased by only 3 mm (3.6%) to a final value of 86 mm for the finer mesh. This demonstrates that numerical convergence was obtained for these computations.

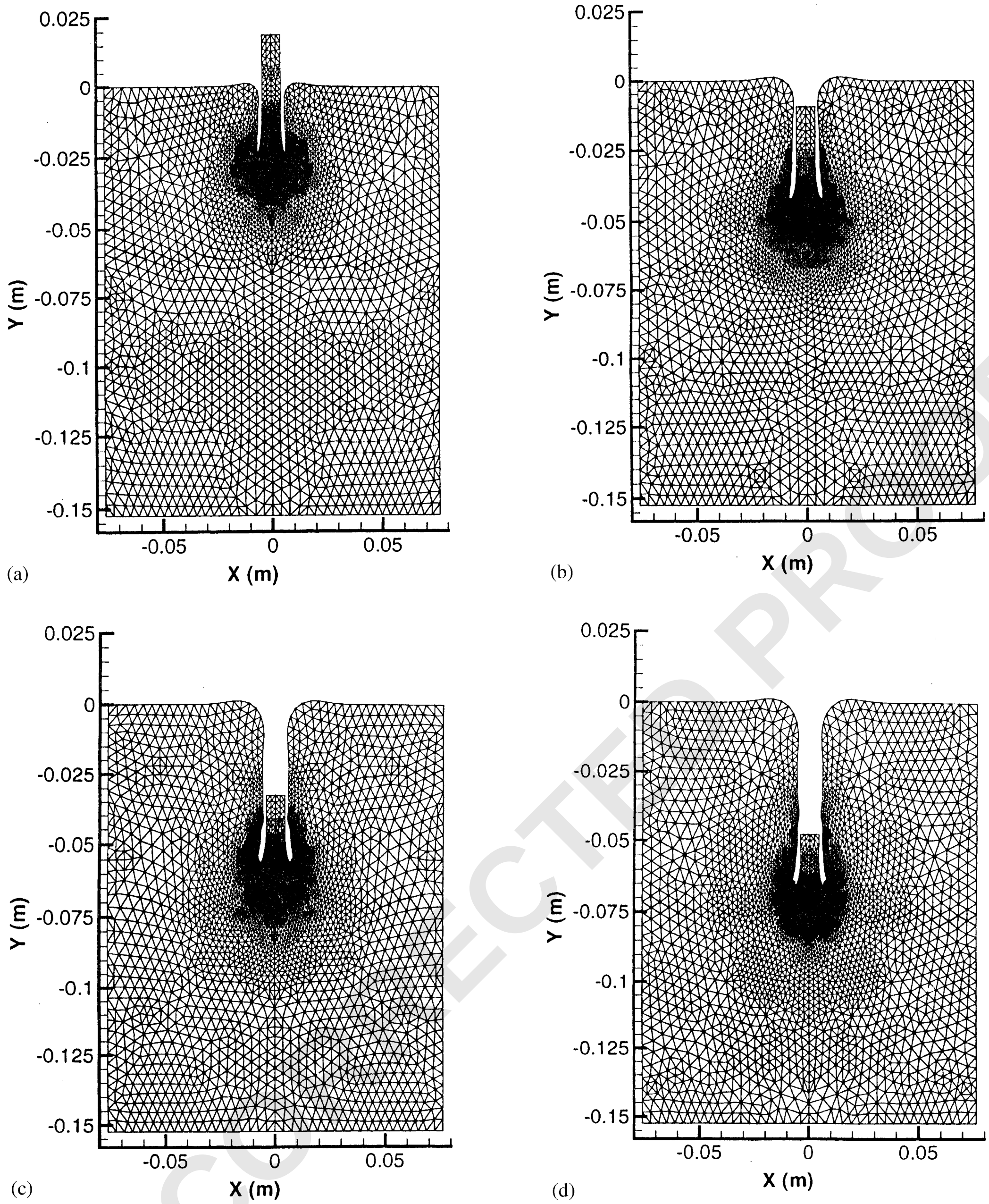

Fig. 2. Deformed finite element meshes at $t = 30$, 60, 90 and 120 μs after impact, $V = 1100$ m/s. Note that adaptive remeshing leads to continuous refinement of the mesh near the penetrator/target interface.

Fig. 3 shows the contour plot of effective plastic strain at $t = 60$ μs after impact, whereas Figs. 4 and 5 show contours of temperature and hydrostatic pressure at two different times during the penetration process. It is clear from these figures that most of the plastic deformation is localized in regions close to the penetrator/target interface. Very large plastic strains and high temperatures

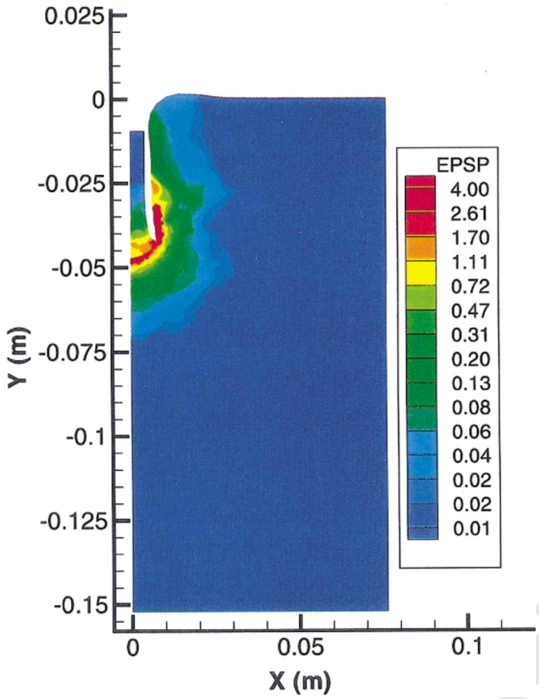

Fig. 3. Contour plot of equivalent plastic strain at $t = 60\,\mu s$ after impact, $V = 1100\,m/s$.

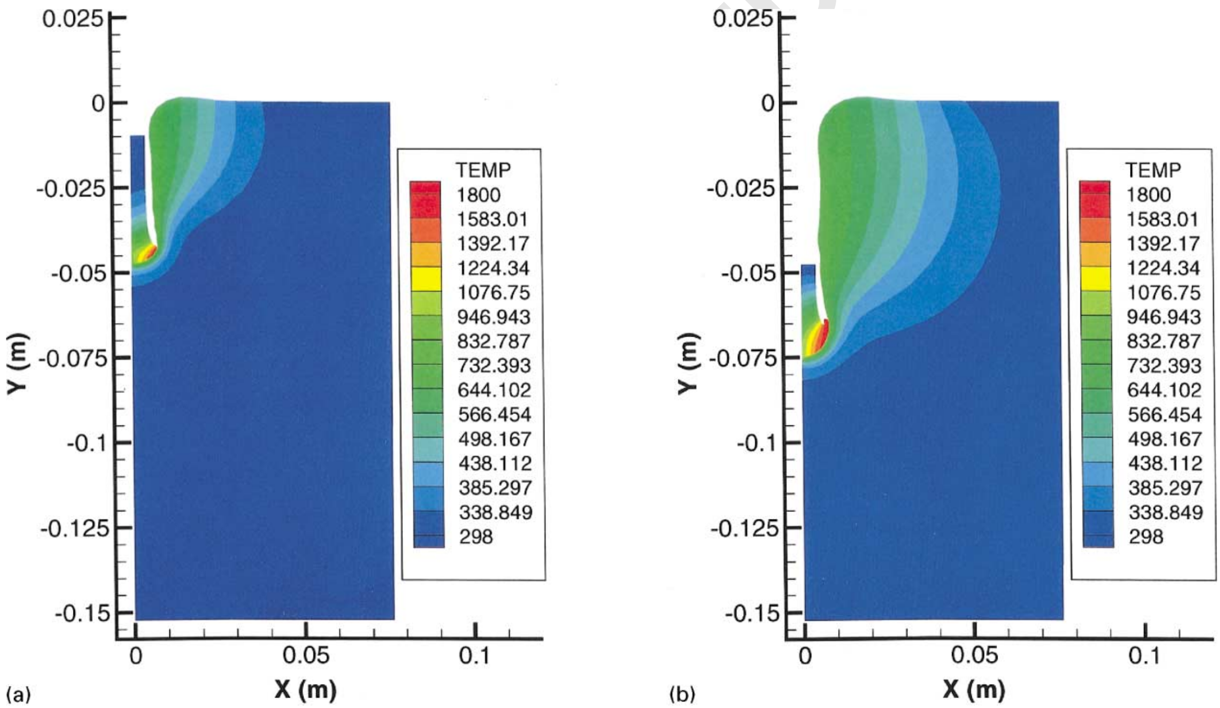

Fig. 4. Contour plots of temperature at $t = 60$ and $120\,\mu s$ after impact, $V = 1100\,m/s$.

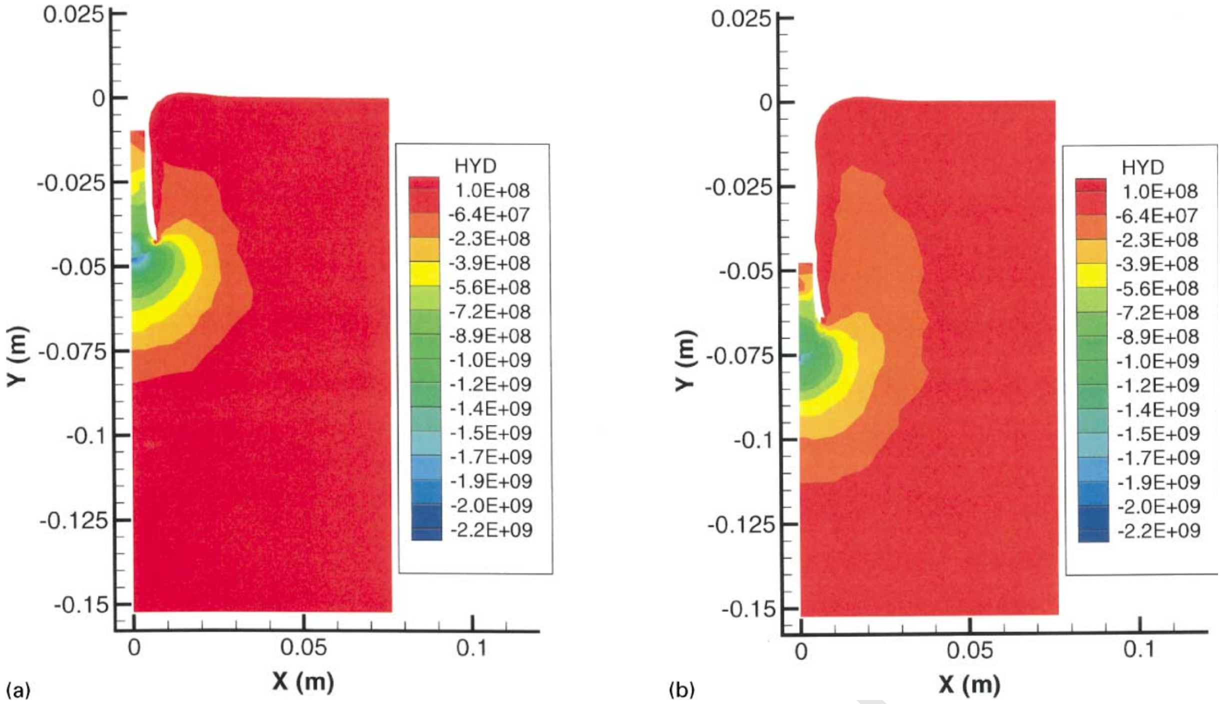

Fig. 5. Contour plots of hydrostatic pressure at $t = 60$ and $120\,\mu s$ after impact, $V = 1100\,m/s$.

are also observed along the rear end of the crater lining. The temperature contours show peak temperatures of the order of 1800 K at the penetrator/target interface. These temperatures are above the melting temperature of both the aluminum and the tungsten alloy. This leads to the formation of an exceedingly narrow boundary layer of molten metal at the penetrator/target interface. The net effect of this mechanism is to defeat friction by lubricating the contact, which is also consistent with the findings of Warren and Forrestal [20] Fig. 5 shows that very high hydrostatic pressures (of the order of 1 GPa) are observed near the penetrator/target interface and that the pressure decays sharply as one moves away from the interface. Note that this high superimposed hydrostatic pressure near the penetrator–target interface (where large deformations and deformation gradients occur) is responsible for the ductile behavior of the target and penetrator materials. The net effect of this hydrostatic pressure is to delay the onset of failure mechanisms such as adiabatic shear localization or void nucleation and growth in the target and penetrator materials.

5.2. The influence of coefficient of friction

The coefficient of friction μ between two surfaces sliding at very high velocities (which occur during ballistic penetration) is generally not well characterized. In order to investigate the influence of coefficient of friction on the computational results, we repeated the above computations with $\mu = 0.2$. This resulted in a total depth of penetration of 79 mm, a decrease of 4.8% from the case where $\mu = 0.01$ (see Run 7 in Table 4). The residual penetrator length and the maximum crater diameter for the run with $\mu = 0.2$ were observed to be the same as that for $\mu = 0.01$ run. Thus, the effect of coefficient of friction on the total depth of penetration is minimal. This hypothesis is also supported by the work of Kraft [21], who showed that the sliding friction accounts for only 3% of the total striking energy of the projectile.

5.3. The influence of thermal softening

We now present the results of a parametric study performed to investigate the influence of thermal softening of the penetrator and target materials on the ballistic performance. Table 4 provides a summary of the six different computational runs performed to investigate the influence of thermal softening parameters on the depth of penetration, residual penetrator length and the maximum crater diameter. The coefficient of friction[1] μ was assumed to be 0.2 for all the six runs. All other parameters used in these simulations were the same as that given in Tables 1–3, except for the value of thermal softening coefficient α and Taylor–Quinney coefficient β which are provided individually in Table 4 for each run.

It is observed that when there is no thermal softening in both the penetrator (WHA) and the target (Al) material (Run 1), then the numerically computed depth of penetration of 104 mm is significantly more than the experimental value of 85 mm. Similarly, the residual penetrator length of 40 mm is about 54% more than the measured value of 26 mm. This indicates that the larger depth of penetration observed for this run is due to a significantly strong penetrator material which does not soften thermally. Also, the maximum crater diameter from numerical simulations is about 34% less than the experimental measurement. These results demonstrate the importance of including thermal softening of the penetrator material in numerical simulations of ballistic penetration.

Run 2 includes linear thermal softening in the target material ($\alpha_{\mathrm{Al}} = 1$) while no softening is assumed for the penetrator material. It is also assumed that no plastic work (in target) gets converted into heat for this run. The softening in the target material is then due to the heat generated at interfaces due to frictional sliding. It is observed that the depth of penetration for this case is significantly larger than all other cases considered. This is again due to a strong penetrator material (with no thermal softening) penetrating into a thermally softening target material. This leads to a residual penetrator length which is significantly larger than that observed experimentally. Note that the maximum crater diameter for this case is the least compared to all other cases. Also note that the inclusion of plastic work in the generated heat (in target) would only further increase the depth of penetration. These results again demonstrate that thermal softening of the penetrator material should be accounted for in numerical simulations of ballistic penetration.

Runs 3 and 4 included linear thermal softening in the penetrator material ($\alpha_{\mathrm{WHA}} = 1$) while no softening was assumed for the target material. Run 3 was performed by assuming no conversion of plastic work into heat ($\beta_{\mathrm{WHA}} = 0$), whereas Run 4 assumed that all the plastic work in the penetrator material gets converted into heat ($\beta_{\mathrm{WHA}} = 1$). For both Runs 3 and 4, it is observed

[1] The larger coefficient of friction (0.2) was used so that an effect of thermal softening due solely to frictional effects could be observed in the parametric study.

that the introduction of a softening mechanism in the penetrator material decreases the depth of penetration in target. Note that due to the inclusion of thermal softening in the penetrator material, there is more plastic flow in the penetrator, which leads to smaller residual penetrator lengths (with a mushroom-shaped nose) and larger crater diameters. Also note that when no conversion of plastic work into heat is assumed (Run 3), the computed depth of penetration (of 79 mm) is close to the experimental value (85 mm). However, the residual penetrator length for this run is more than that observed experimentally. On the other hand, if we assume that all of plastic work gets converted into heat (Run 4), then the computed residual penetrator length matches very well with the experimental results. However, the depth of penetration for this case is much smaller than the experimental measurements. The above results demonstrate the significance of the Taylor–Quinney coefficient β and also strongly suggest that thermal softening of the target materials must be accounted for in numerical computations.

Runs 5 and 6 were performed assuming linear thermal softening ($\alpha = 1$) in both the penetrator and the target material. Whereas for Run 5 it was assumed that no plastic work gets converted into heat ($\beta = 0$), Run 6 assumed that all of the plastic work in the target and penetrator gets converted into heat ($\beta = 1$). It is observed that if the conversion of plastic work into heat is not accounted for (as in Runs 5 and 3), then the inclusion of thermal softening in the target material in Run 5 does not change the DOP appreciably, when compared to Run 3. However, if it is assumed that all of plastic work gets converted into heat (as in Runs 6 and 4), then the inclusion of thermal softening of the target material increases the depth of penetration. Note that we still do not get the experimentally observed values of the depth of penetration and residual penetrator length. This is due to the assumption of linear thermal softening in the penetrator and target materials. In reality, thermal softening is never linear in materials and the use of correct thermal softening coefficients (obtained from experimental data) gives results that correlate fairly well with the experimental measurements (see Run 8 in Table 4). This shows that the temperature dependence of the flow stress is an important factor to be incorporated into computer simulations of ballistic penetration.

5.4. Discussion

It should be noted that we have not incorporated any failure mechanisms such as adiabatic shear localization in our computational simulations. However, our computations assume that the material loses all its strength at its melting temperature, which tacitly accounts for the failure of the material. Our approach of not dealing explicitly with localized shear failures (or other strain instabilities) in the penetrator material is also justified by the experimental work of Zhou et al. [22], who observed that in the presence of superimposed hydrostatic pressures, shear banding in WHA occurs at very large shear strains of the order of 1.0–1.5. Similarly, Yadav and Ramesh [18] reported that the tensile microcracking damage mode that is developed during purely shearing deformations is not observed in either purely compressive or superimposed compression/shear deformations; the superimposed compressive stresses eliminate the microcracking in the material. Recently, Chichili and Ramesh [23] provided experimental evidence of the influence of hydrostatic pressure in delaying the formation of adiabatic shear bands in α-titanium. Note that our computational results show the presence of a very high superimposed hydrostatic pressure near the penetrator/target interface, which could delay (or even prevent) the onset of any shearing instability in the WHA penetrator. Our consideration then of thermal softening in the penetrator material accounts (at least partially) for the loss of material strength that occurs due to material failure. This is due to the fact that the elements with large plastic strain are also heated up significantly. Also note that when using adaptive meshing, even elements with large plastic strain do not get severely distorted. This is due to the fact that during the course of the computations, the mesh is adaptively refined near the penetrator/target interface where intense deformations occur. Thus there is no need to erode elements at the penetrator/target interface.

In contrast, for Lagrangian codes that do not utilize adaptive meshing, severe element distortion occurs and presents difficulties. The distorted elements are generally eroded using criterion such as a critical value of the equivalent plastic strain. Although theoretical considerations call for deletion of only the inverted elements, this would be computationally very inefficient because large element distortion severely reduces the time step size. Therefore, in practice, elements are deleted at smaller values of equivalent plastic strain. Note that different depths of penetration could be obtained for different values of the equivalent plastic strain used for material erosion. Therefore, care should be taken in choosing a critical value of the equivalent plastic strain used for erosion such that the results should approach to the limit where only the inverted elements are deleted for the Lagrangian codes [13]. This generally occurs for values of equivalent plastic strain larger than 2.0. It should be noted that sometimes in Lagrangian formulations, the elements are eroded at smaller values of the equivalent plastic strain to incorporate material failure mechanisms in the computational simulations. Eulerian hydrocodes do not have the problem of excessive mesh distortion. However, even in Eulerian hydrocodes, material elements can be eroded (say when the equivalent plastic strain exceeds a user prescribed erosion strain) to characterize total material failure.

Note that the results presented here are in contrast to the recent work of Rosenberg and Dekel [7] on computational simulations of penetration of tungsten alloy long rods ($L = 300\,\mathrm{mm}$, $L/D = 20$) impacting semi-infinite rolled homogeneous armor (RHA) steel targets at 1.7 km/s. Rosenberg and Dekel used an Eulerian formulation and observed that the introduction of a softening mechanism in the penetrator material lead to an increase in the depth of penetration by about 8% (when compared to the case with no thermal softening in the target and penetrator materials). They concluded that softening of the penetrator head (by melting process) had the strongest influence on penetration depth of long rods. However, our results show that in the absence of other failure mechanisms, the introduction of thermal softening in the penetrator material leads to smaller depths of penetration.

In a previous computational work [5] by the same researchers, Rosenberg and Dekel observed that an increase in the compressive strength of the penetrator material leads to an optimum (maximum) normalized penetration length (P/L). The normalized penetration length was observed to decrease with any further increase in the compressive strength of the penetrator. Similar results have been reported by Partom [24], who obtained an optimum penetration of tungsten alloy rod in RHA steel target for a strength of about 1 GPa (at an impact velocity of 1.5 km/s). It has been suggested by Rosenberg and Dekel [7] that "these codes *predict* that a very strong penetrator is much less efficient than a zero-strength one" due to the inability of the Eulerian model to "remove the *eroded* material from the penetrator nose, increasing penetration resistance in a non-physical manner". Rosenberg and Dekel observed that with the introduction of thermal softening in the penetrator material, the maxima in the penetration versus strength curve disappeared. However, these researchers attributed this to an intrinsically enhanced penetration capability of thermally softening penetrators, rather than due to the mitigation of the "non-physical resistance" at the penetrator/target interface for the thermally softening penetrator. Such an interpretation of the computational results could possibly be facilitated by observations that the ballistic performance of the depleted uranium (DU) penetrators is better than the tungsten heavy alloy (WHA) penetrators at ordnance velocities (800–1800 m/s). This is believed to be due to the apparent ease with which DU can localize adiabatically in shear (because of its higher thermal softening) when compared to WHA [25]. However, in the computational results reported by Rosenberg and Dekel, an increase in the depth of penetration with the inclusion of thermal softening in the penetrator material is observed, even when no failure mechanisms in the penetrator material are accounted for.

It has also been suggested by Rosenberg and Dekel [7] that the maximum equivalent plastic strain could be used as an erosion parameter to account for phenomena such as adiabatic shear banding or other strain instabilities in the WHA penetrator. These researchers observed a significant increase in penetration length on decreasing the equivalent plastic strain for failure in the penetrator material from 1.0 to 0.1, and also indicated the importance of compression failure over the tensile one during ballistic penetration. However, as mentioned earlier, the presence of a high superimposed hydrostatic pressure during ballistic penetration eliminates any microcracking or other failure mechanisms, at least for relatively small values of plastic strains (up to 100%). Note that the differences between our computational results and that of Rosenberg and Dekel are perhaps due to the different failure mechanisms for the two cases. Whereas projectile deformation (mushrooming and softening due to plastic work) is a dominant physical process for our case, erosion (i.e., hydrodynamic process) is the dominant failure mechanism for the cases of Rosenberg and Dekel, the effects of which are modified by softening mechanisms (such as thermal softening or softening via material failure). An interesting extension of the current work would be to perform simulations reported in [7] using the numerical methods reported in the present paper. This would further clarify the influence of thermal softening and failure strain of the penetrator material on the depth of penetration. The results from such an investigation would be reported in a future publication.

6. Summary

A computational study of the penetration of a WHA rod into 6061-T6 aluminum target has been performed using a Lagrangian finite element code with adaptive remeshing. The material parameters chosen for numerical computations were obtained from experimental data. Computational results show excellent agreement with the experimental data. Numerical simulations show that in the absence of any other failure mechanisms, depth of penetration in the target increases with the inclusion of thermal softening in the target material and decreases with the introduction of thermal softening in the penetrator material. It is observed that the coefficient of friction between the penetrator/target surfaces does not influence depth of penetration significantly.

Acknowledgements

This research was supported by the Dow Chemical Company which is gratefully acknowledged. MO is grateful for support from the Army Research Office under grant number DAAH04-96-1-0056.

References

[1] Anderson CE, Mullin SA, Kuhlman CJ. Computer-simulation of strain-rate effects in replica scale-model penetration experiments. Int J Impact Eng 1993;13:35–52.
[2] Hohler V, Stilp A. Hypervelocity impact of rod projectiles with L/D from 1 to 32. Int J Impact Eng 1987; 5:323.
[3] Chen X, Batra RC. Deep penetration of thick thermoviscoplastic targets by long rigid rods. Comput & Struct 1995;54(4):655–70.
[4] Anderson CE, Walker JD. An examination of long rod penetration. Int J Impact Eng 1991;11:481–501.
[5] Rosenberg Z, Dekel E. A computational study of the influence of projectile strength on the performance of long-rod penetrators. Int J Impact Eng 1996;18:671–7.
[6] Rosenberg Z, Dekel E. The relation between the penetration capability of long rods and their length to diameter ratio. Int J Impact Eng 1994;15(2):125–9.
[7] Rosenberg Z, Dekel E. A computational study of the relations between material properties of long-rod penetrators and their ballistic performance. Int J Impact Eng 1998;21:283–96.
[8] Camacho GT, Ortiz M. Adaptive lagrangian modelling of ballistic penetration of metallic targets. Comput Methods Appl Mech Eng 1997;142:269–301.
[9] Yadav S, Ravichandran G. On the penetration resistance of laminated ceramic/polymer structures. Int J Impact Eng, submitted for publication.
[10] PEN2D. User's guide. La Canada, CA: Simulation Technologies Inc., 1998.
[11] Radovitzky, R., Ortiz, M. Error estimation and adaptive meshing in strongly nonlinear dynamic problems. Comput Methods Appl Mech Eng, in press.
[12] Anderson CE, Bodner SR. Ballistic impact: the status of analytical and numerical modeling. Int J Impact Engng 1988;16:9–35.
[13] Chen EP. Finite-element simulation of perforation and penetration of aluminum targets by conical-nosed steel rods. Mech Mater 1990;10:107–15.
[14] Guo Y, Ortiz M, Belytschko T, Repetto EA. Triangular composite finite elements. Int J Num Meth Eng, submitted for publication.
[15] Yadav S, Chichili DR, Ramesh KT. The mechanical response of a 6061-T6 Al/Al_2O_3 metal matrix composite at high rates of deformation. Acta Metall Mater 1995;43(12):4453–64.
[16] Avallone EA, Baumeister T, editors. Mark's standard handbook for mechanical engineers, 10 ed. 1996.
[17] Marsh EA, editor. LASL shock hugoniot data, Los Alamos Series on Dynamic Material Properties. Berkeley, CA: University. of California Press.
[18] Yadav S, Ramesh KT. The mechanical properties of tungsten-based composites at very high strain rates. Mat Sci Eng A 1995;203:140–53.
[19] Hodowany J, Ravichandran G, Rosakis AJ, Rosakis P. On the partition of plastic work into heat and stored energy in metals; Part I: experiments, submitted for publication.
[20] Warren, Forrestal. Effects of strain hardening and strain-rate sensitivity of the penetration of aluminum targets with spherical-nosed rods. Int J Solids Struct 1998;35: 3737-53.
[21] Kraft JM. Surface friction in ballistic penetration. J Appl Phys 1955;26(10):1248–53.
[22] Zhou M, Clifton RJ, Needleman A. Finite element simulations of shear localization in plate impact. J Mech Phys Sol 1994;42:423.

[23] Chichili DR, Ramesh KT. Recovery experiments for adiabatic shear localization: a novel experimental technique. J Appl Mech 1999;66:10–20.
[24] Partom Y. Proceedings of the 15th International Symposium on Ballistics, Jerusalem, Israel, 1995. p. 107–13.
[25] Magness LS, Kapoor D, Dowding R. Novel flow-softening and flow-anisotropy approaches to developing improved tungsten kinetic-energy penetrator materials. Mater Manuf Processes 1995;10:531–40.